

# Journal of Materials Chemistry A

Accepted Manuscript



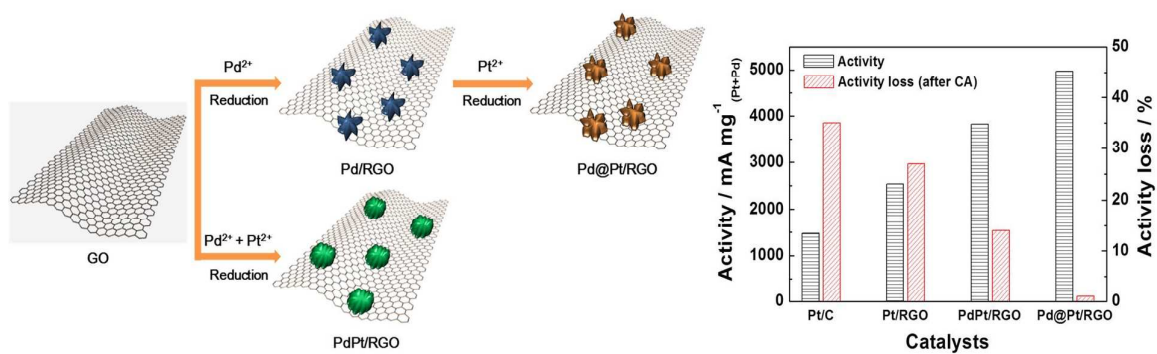
This is an *Accepted Manuscript*, which has been through the Royal Society of Chemistry peer review process and has been accepted for publication.

*Accepted Manuscripts* are published online shortly after acceptance, before technical editing, formatting and proof reading. Using this free service, authors can make their results available to the community, in citable form, before we publish the edited article. We will replace this *Accepted Manuscript* with the edited and formatted *Advance Article* as soon as it is available.

You can find more information about *Accepted Manuscripts* in the [Information for Authors](#).

Please note that technical editing may introduce minor changes to the text and/or graphics, which may alter content. The journal's standard [Terms & Conditions](#) and the [Ethical guidelines](#) still apply. In no event shall the Royal Society of Chemistry be held responsible for any errors or omissions in this *Accepted Manuscript* or any consequences arising from the use of any information it contains.

## Table of Contents



A surfactantless, one-pot reduction approach for Pd@Pt core-shell nano-stars on reduced graphene oxide with enhanced catalytic activity and stability for methanol oxidation in alkaline media.

# Star-shaped Pd@Pt core–shell catalysts supported on reduced graphene oxide with superior electrocatalytic performance

Cite this: DOI: 10.1039/x0xx00000x

Received 00th January 2012,  
Accepted 00th January 2012

DOI: 10.1039/x0xx00000x

www.rsc.org/

Youngmin Kim,<sup>ab</sup> Yuseong Noh,<sup>ab</sup> Eun Ja Lim,<sup>ab</sup> Seonhwa Lee,<sup>bc</sup> Sung Mook Choi<sup>d</sup> and Won Bae Kim<sup>\*abc</sup>

Reduced graphene oxide (RGO)-supported bimetallic Pd–Pt nanostructures with core–shell Pd@Pt (Pd@Pt/RGO) and alloyed PdPt (PdPt/RGO) were prepared by a one-pot reduction approach using L-ascorbic acid for the reduction of both the metal precursors and the graphene oxide supports. Scanning electron microscopy (SEM), transmission electron microscopy (TEM), high-resolution TEM (HR-TEM), and Raman spectroscopy revealed that the three-dimensionally shaped Pd–Pt nanostructures were uniformly deposited onto the reduced graphene oxide surface. The RGO-supported core–shell Pd@Pt and alloyed PdPt catalysts were confirmed and investigated by high-angle annular dark-field scanning TEM (HAADF-STEM) with energy-dispersive X-ray spectroscopy (EDX) in addition to X-ray diffraction (XRD), X-ray photoelectron spectroscopy (XPS), X-ray absorption spectroscopy (XAS), and cyclic voltammetry (CV). With the synergetic effects of the binary Pd–Pt system and the RGO support, these catalysts exhibited considerably enhanced catalytic activities and stabilities for the oxidation of methanol in an alkaline solution compared to monometallic Pt/RGO and commercially available carbon-supported Pt (Pt/C) catalysts. The star-shaped core–shell Pd@Pt/RGO catalysts exhibited the greatest improvement in electrocatalytic performance in terms of current density, onset potential, stability, and charge transfer rate.

## Introduction

Direct methanol fuel cells (DMFCs) are considered to be a promising energy source for portable electronics, with the advantages of a high energy density (6100 Wh kg<sup>-1</sup>), easy handling of liquid fuels, low operating temperatures, and simple system design.<sup>1</sup> More recently, research interest in alkaline DMFCs that employ anion-exchange membranes has increased due to their facilitated kinetics for electrode reactions in alkaline media as compared to those in acidic media.<sup>2</sup> Currently, platinum (Pt) has been accepted as the most active catalyst for methanol electrooxidation in both acid and alkaline DMFCs. However, the high cost of Pt and poisoning of the Pt surface via strong adsorption of CO or intermediate species generated during the methanol oxidation reaction (MOR) are the major impediments to the successful application of DMFCs.

To improve the catalytic performance of Pt and to reduce the amount of Pt used, bimetallic catalysts in the forms of alloys and core–shell structures have been fabricated.<sup>3–10</sup> Among the various metals investigated, palladium (Pd) is not only much less expensive than pure Pt, but Pd itself also exhibits potentially high catalytic activity with good resistance to CO poisoning, especially during alcohol oxidation in alkaline media.<sup>11,12</sup> In this regard, Pd–Pt bimetallic nanostructures could be a promising efficient binary electrocatalyst for methanol

oxidation. In particular, Pd@Pt core–shell nanostructures have recently attracted attention because they can exhibit better catalytic performance than pure Pt even though a much smaller amount of Pt is used.<sup>13–16</sup>

The ability to control and change the shape and morphology of bimetallic nanostructure catalysts can provide an effective approach to the development of highly active electrocatalysts because it could change the crystallographic facets exposed on the surface; the exposed crystallographic facets strongly affect the catalytic properties of the bimetallic nanostructures, which are largely dependent on their surface structure and surface composition.<sup>17</sup> Numerous literature studies have reported that the electrocatalytic activities and stabilities can be enhanced through manipulation of the morphology of nanostructures such as nanocubes,<sup>18–20</sup> nanocages,<sup>21</sup> nanowires,<sup>22–25</sup> nanotubes,<sup>26–28</sup> nanoframes,<sup>29</sup> dendrites,<sup>30–32</sup> or porous nanostructures.<sup>33,34</sup>

The catalyst supports also play critical roles in determining the catalytic activity and stability. Graphene, as a two-dimensional atomic layer of carbon, has emerged as a new class of catalyst support material for dispersed metal/metal oxide nanoparticles because of its high specific surface area (theoretically, 2630 m<sup>2</sup> g<sup>-1</sup>), high electrical conductivity (10<sup>3</sup>–10<sup>4</sup> S m<sup>-1</sup>), good chemical/thermal stability, and strong adhesion to metal/metal oxide nanoparticles.<sup>35,36</sup> These unique properties are adequate to improve the dispersion of nano-sized

electrocatalysts, facilitate charge transport at the electrode surface, and maintain a stable catalyst structure. Moreover, graphenes, when doped by other heteroatoms like boron<sup>37</sup> and nitrogen<sup>38–40</sup>, were used as metal-free electrocatalysts. In general, graphene supports can be prepared in large quantities through the oxidative exfoliation of common graphite to graphene oxide (GO) and the subsequent chemical/thermal reduction of GO to reduced graphene oxide (RGO).<sup>41,42</sup> Two reduction routes for the preparation of metal/RGO composites exist: the reduction of metal salts supported on the as-prepared RGO (or graphene) and co-reduction of metal salts and GO in a one-pot manner. From the viewpoint of simplicity, the latter method appears to be more attractive. Recent studies have demonstrated that L-ascorbic acid (AA) is an effective and environmentally benign reductant for such simultaneous reduction of the metal salts and GO to form metal/RGO composites.<sup>43,44</sup> With respect to this strategy, however, the literature contains few reports on the decoration of core-shell Pd@Pt and alloy PdPt nanoparticles on the surface of RGO via a surfactant-free one-pot route for their application as MOR catalysts in alkaline environments.

In this work, RGO-supported bimetallic Pd–Pt nanostructures with different core-shell (Pd@Pt/RGO) and alloy (PdPt/RGO) structures were prepared via a simple, surfactantless, one-pot synthetic route. For comparison purpose, RGO-supported monometallic Pt (Pt/RGO) was also prepared using the same method. AA was used as a co-reducing agent for both the metal precursors and the GO. Notably, no surfactants were used in the preparation procedure described in this work. Surfactants, which are typically used for tuning the shapes of metal nanostructures in solution, can deleteriously affect the electrocatalytic performance of nanostructures. Interestingly, in the absence of surfactants, different shapes of clustered nanostructures (i.e., star-shaped Pd@Pt core-shell and alloyed PdPt) or nanoparticle (i.e., Pt nanoparticles) were produced on the RGO sheets under the experimental synthesis conditions. The physicochemical and electrochemical characteristics of the prepared nanocomposites were systematically investigated. The synthesized RGO-supported nanostructures exhibited better catalytic activity toward MOR in an alkaline medium than did the commercial C-supported Pt nanoparticles (Pt/C), and the Pd@Pt/RGO exhibited the highest electrocatalytic activity and stability among the investigated catalysts.

## Experimental

### Chemicals

Palladium(II) chloride (PdCl<sub>2</sub>, 99.0%, Kojima Chemicals, Japan), potassium tetrachloroplatinate(II) (K<sub>2</sub>PtCl<sub>4</sub>, 98%, Sigma-Aldrich), L-ascorbic acid (C<sub>6</sub>H<sub>8</sub>O<sub>6</sub>, 99+%, Sigma-Aldrich), deionized water (DI water, 18 MΩ·cm, Millipore), sodium hydroxide (NaOH, Samchun Pure Chemical), graphite (Carbonix, Korea), Pt/C (20 wt%, Alfar Aesar), methanol (HPLC grade, Fischer Scientific Korea), and ethanol (HPLC grade, Fischer Scientific Korea) were purchased from the specified suppliers and were used as received without further purification.

### Synthesis of RGO supported Pd@Pt, PdPt, and Pt electrocatalysts

Graphite oxide was synthesized from natural graphite by the modified Hummers and Offeman method.<sup>45</sup> The synthesized graphite oxide was dispersed in DI water (2 mg·ml<sup>-1</sup>) and ultrasonicated for 30 min to obtain exfoliated GO. For a typical synthesis of Pd@Pt/RGO, PdCl<sub>2</sub> (8.4 mg in 4 ml DI water) was

first added to 20 ml of the dispersed GO solution. Then, 1 ml of 5 M NaOH solution and AA (500 mg in 5 ml DI) were added, and the mixture was aged for 24 h at room temperature. Subsequently, K<sub>2</sub>PtCl<sub>4</sub> (10.6 mg in 4 ml DI water) was added; the mixture was heated at 90 °C for 1 h and then allowed to cool to room temperature. The resulting dispersion was separated and purified with water and ethanol by centrifugation and was dried via the freeze-drying method to minimize aggregation of RGO sheets.

For the synthesis of PdPt/RGO and Pt/RGO, the mixture of K<sub>2</sub>PtCl<sub>4</sub> (10.6 mg in 4 ml DI water) and PdCl<sub>2</sub> (8.4 mg in 4 ml DI water) or K<sub>2</sub>PtCl<sub>4</sub> (21.2 mg in 8 ml DI water) were added to 20 ml of the dispersed GO solution, respectively. The resulting solution was then treated using the same procedures used in the synthesis of Pd@Pt/RGO.

### Materials characterization

SEM images of as-produced samples were obtained using a JEOL-JSN7500F operated at 5 kV. HRTEM images, HAADF-STEM images, elemental mapping, and EDX analysis were performed using a Tecnai G2F30 microscope operated at 200 kV. The compositions (metal loading and element ratio) of RGO supported catalysts were measured by inductively coupled plasma emission spectrometry (ICP-AES, Perkin Elmer) and thermogravimetric analyzer (TGA, TGA-50H, Shimadzu). To investigate crystallographic structures of the samples, powder XRD was conducted on a Rigaku Rotaflex (Ru-200B) X-ray diffractometer equipped with a Ni filter and a Cu Kα (λ = 1.5405 Å) radiation source operated at 40 kV and 100 mA. Raman spectra were collected on a RENISHAW inVia Raman microscope with 514 nm Ar<sup>+</sup> laser excitation. The XPS was performed on a MULTILAB 2000 system equipped with a monochromatic Al Kα X-ray source (E = 1486.6 eV). The binding energy of the C 1s peak at 284.6 eV was taken as an internal standard. XAS measurements, including the X-ray absorption near edge spectra (XANES) and extended X-ray absorption fine structure (EXAFS), were carried out on 7D beamline of the Pohang Accelerator Laboratory (PLS-II, 3.0 GeV, Korea) using a Si (111) double crystal monochromator. The spectra were measured at room temperature in a transmission mode for the L<sub>3</sub> edge of Pt (11564 eV) and K edge of Pd (24350 eV) under the ambient condition. Energy calibration was performed using a standard metal foil. The XAS data were processed and analyzed following those described in detail elsewhere<sup>4,46</sup> with the IFEFFIT software package (ATHENA and ARTEMIS programs).<sup>47</sup> The data from Pt L<sub>3</sub> and Pd K edges for bimetallic Pd–Pt catalysts (i.e., PdPt/RGO and Pd@Pt/RGO) were fitted simultaneously by constraining the interatomic distance (R) of R<sub>Pt–Pd</sub> = R<sub>Pd–Pt</sub>, the Debye–Waller factor (σ<sup>2</sup>) of σ<sup>2</sup><sub>Pt–Pd</sub> = σ<sup>2</sup><sub>Pd–Pt</sub>, and the coordination number (N) N<sub>Pt–Pd</sub> = (X<sub>Pd</sub>/X<sub>Pt</sub>)N<sub>Pd–Pt</sub>, where X<sub>Pd</sub>/X<sub>Pt</sub> is the molar ratio of Pd to Pt in the nanoparticles, and R<sub>A–B</sub>, σ<sup>2</sup><sub>A–B</sub>, and N<sub>A–B</sub> is the R, σ<sup>2</sup>, and N of atom B around A, respectively. The parameters of amplitude reduction factors (S<sub>0</sub><sup>2</sup>) were set to the values of 0.862 (Pt L<sub>3</sub> edge) and 0.802 (Pd K edge) determined from fitting the corresponding metal foils. Only the k range of 3 – 13 Å<sup>-1</sup> and R range of 1.8 – 3.1 Å were fitted on k<sup>3</sup> weighted EXAFS data with the first-shell single scattering paths.

### Electrochemical measurements

All electrochemical tests were performed at room temperature in a standard three-electrode cell connected to a Solartron Analytical instrument (AMETEK model 1470E). A Pt wire was used as the counter electrode, and a saturated calomel electrode

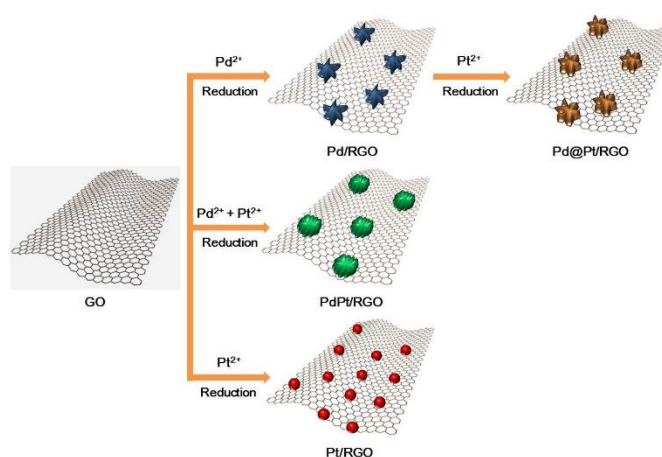
(SCE) was used as a reference electrode. The working electrode was fabricated on a glassy carbon electrode with a diameter of 3 mm. To prepare catalyst inks, each catalyst was suspended in ethanol and sonicated for 30 min. Next, 5  $\mu\text{l}$  of the catalyst ink (1 mg  $\text{ml}^{-1}$ ) was dropped by a micropipette onto the glassy carbon surface. After the catalyst was loaded, the working electrode was dried at room temperature to remove the ethanol. Cyclic voltammetry (CV) curves were collected in the potential window between  $-0.95$  and  $0.25$  V at a scan rate of  $50$   $\text{mV s}^{-1}$  in an  $\text{N}_2$ -purged  $0.5$  M NaOH or  $0.5$  M methanol +  $0.5$  M NaOH electrolyte solution. Chronoamperometry (CA) of each sample was performed for up to 3600 seconds at a fixed voltage of  $-0.25$  V. Electrochemical impedance spectroscopy (EIS) measurements were recorded in a frequency range from  $10$  kHz to  $1$  Hz with AC amplitude of  $5$  mV.

## Results and discussion

The synthetic routes for the preparation of various metal/RGO composites are summarized in Scheme 1. To prepare core-shell Pd@Pt on RGO, GO and  $\text{Pd}^{2+}$  in an aqueous mixture were first reduced using AA as a reductant to form Pd/RGO composites, and  $\text{Pt}^{2+}$  was subsequently added to grow a Pt shell layer on the surface of the pre-formed Pd nanocrystals. Interestingly, the Pd nanocrystals that formed on RGO exhibited a star-shaped morphology, with several dendritic branches, and the shape of the core-shell Pd@Pt particles was similar to the shape of the Pd particles. Generally, the growth of metal nanoparticles involves nucleation followed by ripening of the small cluster. Based on the previous literatures<sup>14,48,49</sup>, plausible growth process for star-shaped Pd/RGO can be proposed. At the initial stage of reaction, nucleation of Pd occurs and small Pd nuclei are formed on GO, followed by evolution of these small Pd nuclei to larger primary Pd nanocrystals, and finally converted into star-shaped Pd nanostructures by Ostwald ripening. It was reported that AA might promote the formation of branched nanocrystals<sup>50-52</sup>. The pH value also can influence the nucleation and growth kinetics of the metal nanoparticles. For instance, a higher pH value was found to decrease the reduction rate. For star-shaped Pd@Pt/RGO, the pre-formed Pd clusters on RGO were used as seeds to generate core-shell nanostructures with Pt shells through successive overgrowth. The close matching between the lattice parameter of Pt and Pd and the slow reduction rate associated with the mild reduction ability of AA played a key role in achieving the epitaxial growth of Pt shells on Pd seeds.<sup>53</sup> However, simultaneous reduction of  $\text{Pd}^{2+}$  and  $\text{Pt}^{2+}$  produced foam-like PdPt alloy structures on RGO. Different reduction rates of the metal precursors may play a certain role in the different structural evolution of the particles.<sup>54</sup>

The morphology of the GO, Pd@Pt/RGO, PdPt/RGO, and Pt/RGO was examined using SEM (Figure S1 in ESI). Crumpled sheet-like morphology of GO and RGO can be observed in all of the samples. No nanoparticles were observed at the surface of GO. However, well-distributed nanoparticles were observed in the samples of Pd@Pt/RGO, PdPt/RGO, and Pt/RGO.

TEM images (Figures S2A-B) of the Pd/RGO sample, which was used as the seed for Pd@Pt/RGO, revealed that Pd particles consisted of star-shaped clusters with an average size of  $22.3 \pm 3.2$  nm that are composed of 5-7 primary Pd grains. The HRTEM image of individual Pd branches shows their single-crystalline structure (Figure S2C), and the EDX



**Scheme 1.** Schematic illustration of the synthesis procedure for Pd@Pt/RGO, PdPt/RGO, and Pt/RGO with different morphologies.

spectrum reveals that they are mainly composed of pure Pd (Figure S2D). Copper peaks in the EDX spectrum originated from the copper TEM grid.

Figures 1A-B show TEM images of the Pd@Pt core-shell particles supported on an RGO sheet at different magnifications. The sizes of the Pd@Pt particles are distributed from approximately  $15$  to  $35$  nm, with an average size of  $25.9 \pm 3.4$  nm. The individual particle has a star-like morphology, as shown in Figure 1C. The HRTEM image of Pd@Pt/RGO in Figure 1D shows that the Pd@Pt particles are highly crystallized, as indicated by the well-defined fringe pattern. The corresponding FFT pattern indicates that the individual branch is composed of single nanocrystals (inset of Figure 1D). The interplanar spacing calculated from the FFT analysis of HRTEM image was  $2.25$  Å, which corresponds to that of the (111) plane of face-centered-cubic (fcc) Pt. The EDX analysis confirms the presence of both Pd and Pt in the Pd@Pt core-shell nanoparticles (Figure 1E). The bulk atomic ratio of the Pd:Pt was measured to be 66:34, which is close to the ratio of metal precursors originally added (65:35) and also consistent with the ICP-AES results (69:31). The weight percentages of C, Pd, and Pt confirmed by ICP-AES analysis are 79.57, 11.30, and 9.13%, respectively. The HAADF-STEM image of a single Pd@Pt particle and the corresponding elemental maps reveal that Pd could only be found in the core region, whereas Pt was distributed throughout the entire particle, which suggests a core-shell structure (Figure 1F).

Figures 2A-B shows TEM images of PdPt alloy particles on the RGO sheets, and Figure 2C shows that the individual particle has a spherical foam-like morphology with a size of approximately  $23.0 \pm 3.5$  nm. The PdPt particles appear to compose numerous single crystals, as evident in the HRTEM image and the corresponding FFT pattern in Figure 2D and the inset of Figure 2D, respectively. The interplanar spacing between adjacent lattice fringes was  $2.23$  Å, corresponding (111) plane of PdPt alloy. It should be noted that the interplanar spacing of PdPt/RGO was smaller than that of Pd@Pt/RGO, which could be due to the lattice contraction from the alloy formation. The EDX spectrum in Figure 2E shows that both Pd and Pt are present that the bulk Pd:Pt atomic ratio is ca. 64:36, which is also approximately consistent with the metal precursor ratio originally added (65:35) and the results of the ICP-AES analysis (67:33). The weight percentages of C, Pd, and Pt confirmed by ICP-AES analysis were 78.89, 11.21, and 9.9%, respectively. The elemental maps collected in HAADF-STEM

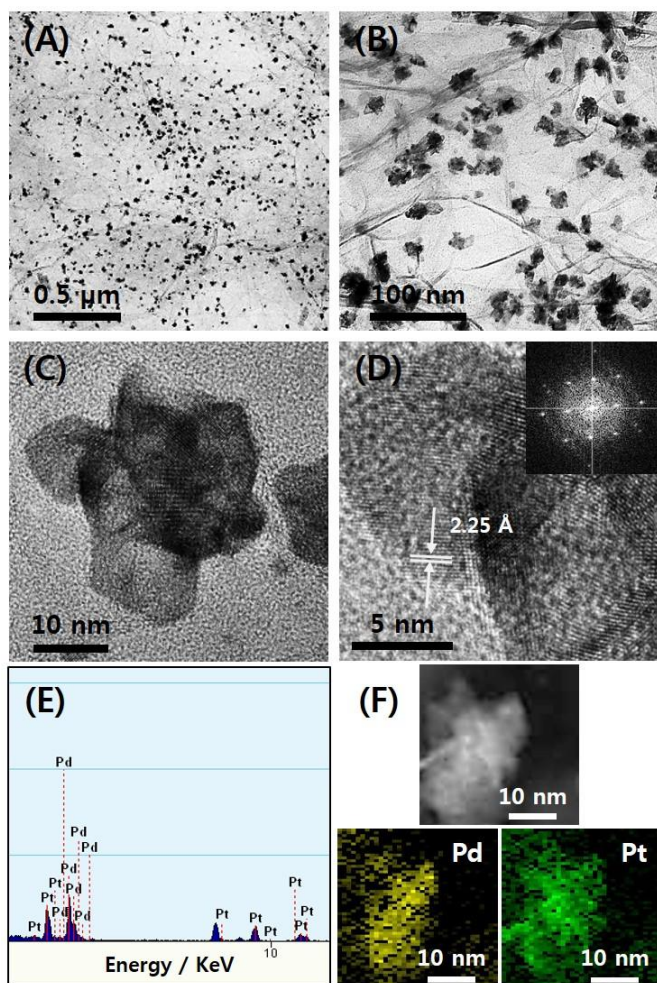


**Figure 1.** (A-B) TEM images of Pd@Pt/RGO at different magnifications, (C-D) an HR-TEM image of individual Pd@Pt particles on RGO, (E) an EDX spectrum of Pd@Pt/RGO, (F) HAADF-STEM images of Pd@Pt/RGO and corresponding elemental maps of Pd and Pt. The inset in (D) shows the FFT pattern of the HRTEM image.

mode reveal that both Pd and Pt are evenly distributed within the particle, which suggests that a homogeneous alloy structure of PdPt is formed on the RGO (Figure 2F).

RGO-supported monometallic Pt was also prepared using the same synthesis conditions described in the experimental section, and the product was characterized by TEM, HRTEM and EDX analyses (Figure S3). Spherical shapes of Pt nanoparticles with a small size of ca.  $3.0 \pm 0.6$  nm were finely dispersed on the surface of the RGO sheets (Figures S3A-B). The HRTEM image and EDX spectra of the Pt nanoparticles indicate that they are single crystals of pure Pt (Figures S3C-D).

To quantify the metal loading on the RGO support, TGA analysis was carried out under air atmosphere as shown in Figure S4. On the basis of TGA analysis, the metal loadings of the Pt/RGO, PdPt/RGO, and Pd@Pt/RGO catalysts were 22.5, 23.6, and 23.3 wt%, respectively, indicating that the RGO-supported catalysts used in this experiments have similar amount of metal loading.

XRD patterns of GO, Pt/RGO, PdPt/RGO, and Pd@Pt/RGO are displayed in Figure 3A. The intense peak centered at  $10.9^\circ$  corresponds to the (002) plane and the peak at  $42.5^\circ$  corresponds to the (001) plane of GO. The broad peak appeared around  $23^\circ$  suggests the presence of unoxidized graphitic

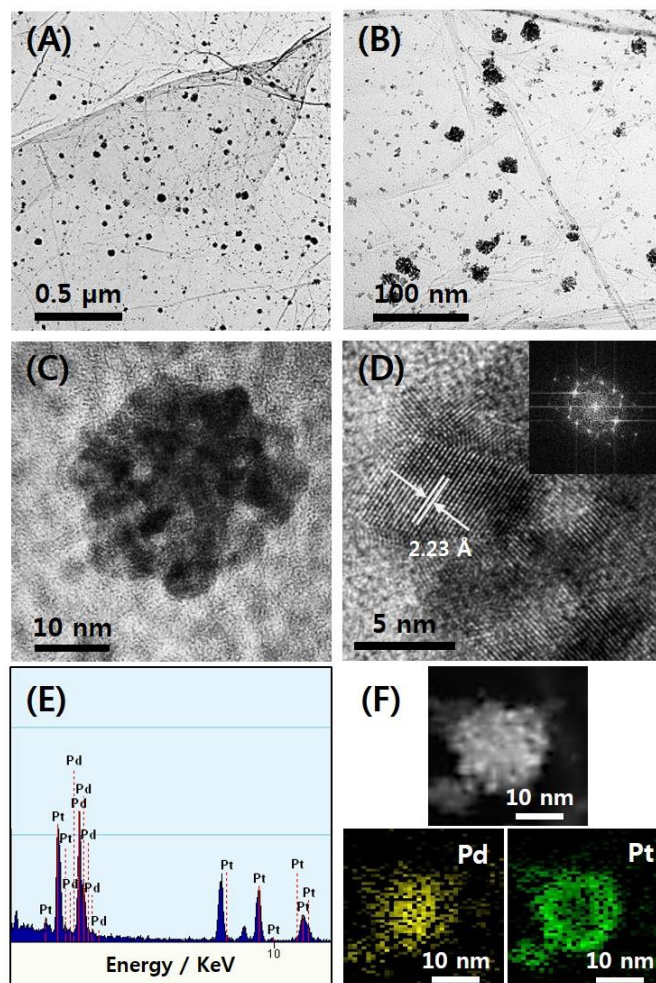


**Figure 2.** (A-B) TEM images of PdPt/RGO at different magnifications, (C-D) an HR-TEM image of an individual PdPt particle on RGO, (E) the EDX spectrum of PdPt/RGO, (F) HAADF-STEM images of PdPt/RGO and the corresponding elemental maps of Pd and Pt. The inset in (D) shows the FFT pattern of the HRTEM image.

domains<sup>55</sup> and amorphous carbon phase<sup>56</sup>. After chemical reduction by AA to produce the RGO-supported catalysts, the sharp diffraction peak of GO at  $10.9^\circ$  disappeared in the XRD patterns, implying partial removal of the oxygen functional groups.<sup>57</sup> In the XRD patterns of RGO-supported catalysts, the first broad peak located at ca.  $21.5^\circ$  is attributed to the (002) plane of the hexagonal structure of reduced graphene oxide. The other characteristic peaks exhibit the fcc lattice structure of Pt and Pd, corresponding to the (111), (200), and (220) planes. Owing to the similarity of crystalline structures between Pd and Pt (lattice mismatch ratio of Pd/Pt is only 0.77%), the difference in the XRD patterns for Pd and Pt is not distinct. The diffraction peaks of PdPt/RGO exhibit a little shift to higher value as compared to that of Pt/RGO. For instance, the (111) peak from the Pt/RGO locates at  $39.6^\circ$ , whereas the corresponding peak from the PdPt/RGO shifts to  $40.0^\circ$ , indicating the decrease in lattice constant. The decrease of lattice constant can be ascribed to the substitution of Pt with Pd, leading to the contraction of the fcc lattice. The (111) diffraction peak of PdPt/RGO appears at a slightly higher angle than that of Pd@Pt/RGO ( $39.8^\circ$ ), which indicates a difference in the extent of alloying and/or in the structures.<sup>58,59</sup> The average crystallite sizes can be calculated on the basis of the

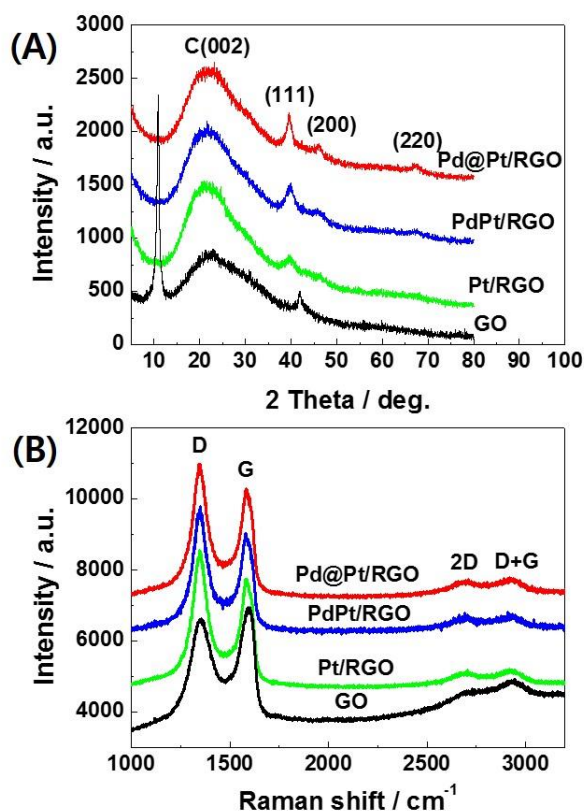


**Figure 3.** (A) XRD and (B) Raman spectra of GO, Pt/RGO, PdPt/RGO, and Pd@Pt/RGO.

broadening of the (111) diffraction peaks according to the Scherrer formula.<sup>60</sup> The calculated crystallite sizes for Pt, PdPt, and Pd@Pt particles deposited on the RGO were approximately 2.5, 4.4, and 6.2 nm, respectively. The calculated size of the Pt nanoparticles matched well with the values determined from TEM analysis, whereas the XRD-based particle sizes of the PdPt and Pd@Pt crystallites were much smaller than the cluster dimensions observed in the TEM images. Given these differences, we speculate that the PdPt and Pd@Pt nanostructures were formed by several primary nanoparticles in a size range of 4–6 nm.

Raman spectra (Figure 3B) also supported the XRD results. The frequencies of the D and G bands were approximately 1354 and 1597  $\text{cm}^{-1}$ , respectively. The D band is associated with the order/disorder of the graphite edge, and the G band is an indicator of the graphitic stacking structure. High D/G intensity ratios indicate a high degree of disorder/exfoliation.<sup>61</sup> The D/G ratios for Pt/RGO, PdPt/RGO, and Pd@Pt/RGO were calculated to be approximately 1.24, 1.24, and 1.20, respectively; these ratios are significantly greater than the ratio of GO ( $\sim 0.89$ ), which indicates that GO was successfully reduced to RGO.<sup>62,63</sup> The 2D peak and the D+G peak were observed at about 2695 and 2925  $\text{cm}^{-1}$ , respectively. The 2D peak is sensitive to the stacking order of the graphene sheets along the c-axis as well as to the number of layers, which broadens with an increase of the layer number. Thus, it is expected that the samples contain highly disordered and randomly arranged multiple layer carbon sheets.

We performed XPS measurements of the RGO-supported Pt, PdPt, and Pd@Pt catalysts to obtain information related to their surface chemistry. Figures 4A and B show the XPS core-level

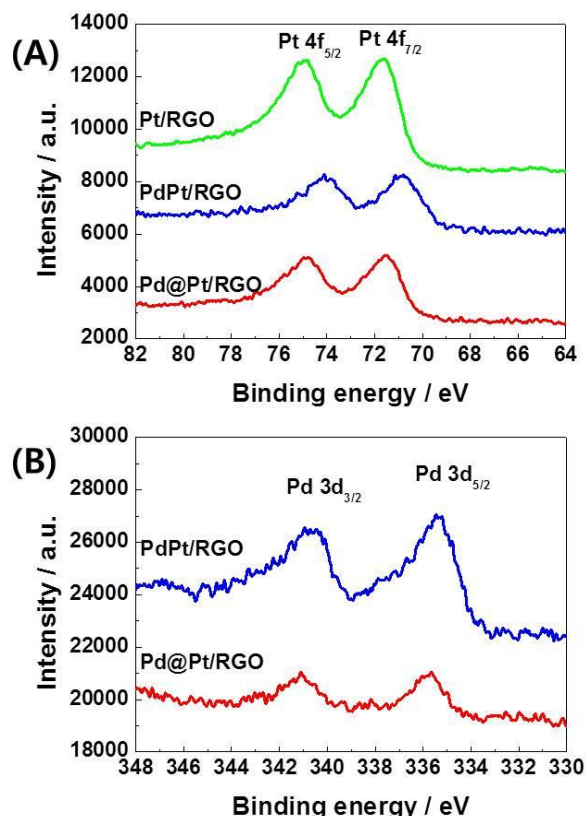


**Figure 4.** XPS spectra of (A) Pt 4f and (B) Pd 3d for the Pt/RGO, PdPt/RGO, and Pd@Pt/RGO.

spectra for the Pt 4f and Pd 3d regions, respectively. To verify the specific valence states of the catalysts, the obtained XPS peaks were curve-fitted, as shown in Figure S5. The BEs of core electrons and relative amounts of different oxidation states for the Pt 4f<sub>7/2</sub> and Pd 3d<sub>5/2</sub> regions are reported in Table 1. It was found that the predominant surface species in the prepared catalysts are the metallic state of Pt and Pd, and relatively small amounts of the oxidized species are present. The binding-energy values of the metallic Pt 4f<sub>7/2</sub> peaks in PdPt/RGO and Pd@Pt/RGO are negatively shifted compared with the value for the Pt/RGO (71.51 eV), which implies that the electronic structure of Pt was modified by the addition of Pd (Table 1). It is to be noted that the Pt 4f<sub>7/2</sub> binding energy for PdPt/RGO (70.68 eV) shifted to a lower binding energy compared to the Pd@Pt/RGO (71.43 eV), implying that an electronic modification of Pt in PdPt/RGO is more significant than that in the Pd@Pt/RGO, which may be due to the PdPt alloy surface. The surface Pd:Pt atomic ratio of PdPt/RGO calculated from the XPS spectra was 67:33, which is also consistent with the bulk atomic ratio determined by ICP (67:33) and by EDX (64:36); these results indicate the formation of a composite alloy throughout the particles in the case of PdPt/RGO. However, the surface Pd:Pt atomic ratio of the core-shell Pd@Pt/RGO was 32:68, which shows a large discrepancy with the bulk atomic ratio determined by ICP (69:31) and EDX (66:34). This discrepancy indicates that the surface is significantly rich in Pt. These findings combined with elemental mapping strongly support the suggestion that the PdPt/RGO has an alloy structure and that the Pd@Pt/RGO has a core-shell structure, even though their overall compositions are the same. Figures S6A and B show the deconvoluted C1s

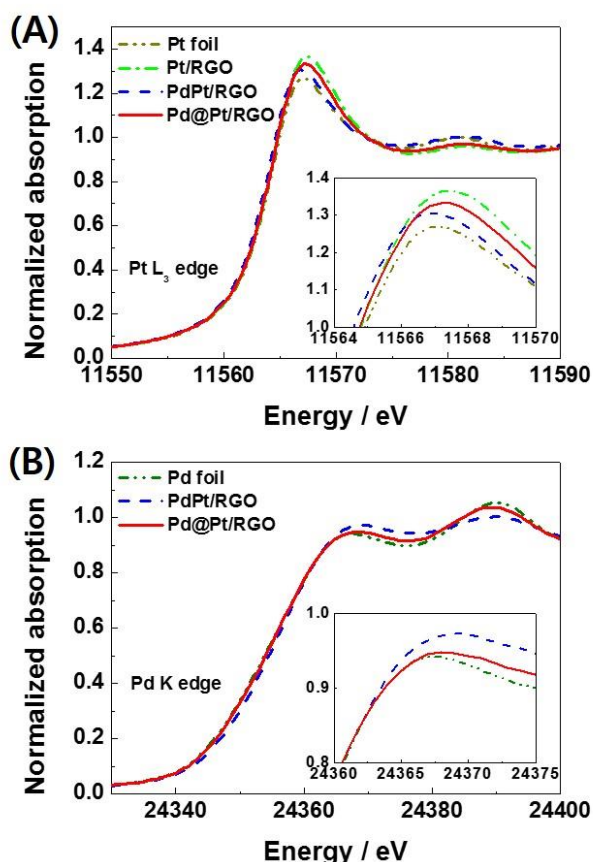


**Figure 5.** XANES spectra of (A) Pt  $L_3$  edge and (B) Pd K edge for Pt/RGO, Pd/RGO, PdPt/RGO, and Pd@Pt/RGO with their corresponding metal foils.

XPS spectra of GO and Pd@Pt/RGO, respectively. Importantly, the intensities of the peaks associated with oxidized carbon species such as C-O and C=O of the Pd@Pt/RGO sample were appreciably reduced compared to those in the spectrum of the GO sample, which implies that GO to RGO were chemically reduced during the co-reduction process in the preparation of Pd@Pt/RGO.<sup>64</sup> The reduction level in the RGO sheet was estimated by the XPS analysis. As shown in Figure S7, the O peak intensity of Pd@Pt/RGO was obviously decreased in as compared with GO. The carbon to oxygen (C/O) atomic ratio of RGO in Pd@Pt/RGO was remarkably increased up to 8.2, which is much higher than that of GO (2.0), indicating the oxygen containing group was largely removed after the reduction of GO by AA. Moreover, this reduction level is higher than many other reported methods<sup>65–69</sup>. Therefore, the XPS results also support the successful formation of RGO, along with the results of the XRD and Raman analyses.

XAS is a powerful technique to evaluate the local electronic and geometric structures of X-ray absorbing atoms. Figure 5 shows the normalized XANES spectra recorded at the Pt  $L_3$  edge (Figure 5A) and Pd K edge (Figure 5B) for the prepared catalysts. Overall Pt  $L_3$  and Pd K edge XANES shapes of the RGO-supported catalysts are similar to those of the corresponding metal foils, which indicates that the Pt and Pd in the catalysts are of predominantly metallic states. The white line (WL), which is a strong peak above the edge energy position, is directly related to the density of vacant  $d$  orbital states.<sup>70,71</sup> It corresponds to  $2p_{3/2} \rightarrow 5d$  transition at the Pt  $L_3$  edge and  $1s \rightarrow 4d$  transition at the Pd K edge, respectively. The

**Table 1.** Binding energies and the compositions of the RGO-supported catalysts measured from XPS, ICP, and EDX.

Catalyst	Pt $4f_{7/2}$ BE (eV)		Pd $3d_{5/2}$ BE (eV)		Pd:Pt <sup>c</sup>	Pd:Pt <sup>d</sup>	Pd:Pt <sup>e</sup>
	Pt <sup>0</sup>	Pt <sup>2+</sup>	Pd <sup>0</sup>	Pd <sup>2+</sup>			
Pt/RGO	71.51 (74.0) <sup>a</sup>	72.40 (26.0) <sup>a</sup>	-	-	-	-	-
PdPt/RGO	70.68 (81.7) <sup>a</sup>	71.49 (18.3) <sup>a</sup>	335.32 (71.9) <sup>b</sup>	336.75 (28.1) <sup>b</sup>	67:33	67:33	64:36
Pd@Pt/RGO	71.43 (79.5) <sup>a</sup>	72.40 (20.5) <sup>a</sup>	335.68 (82.2) <sup>b</sup>	336.33 (17.8) <sup>b</sup>	32:68	69:31	66:34

<sup>a</sup> Relative % of the Pt<sup>0</sup> and Pt<sup>2+</sup> species.

<sup>b</sup> Relative % of the Pd<sup>0</sup> and Pd<sup>2+</sup> species.

<sup>c</sup> Surface atomic ratio calculated from XPS analysis by using peak areas normalized on the basis of sensitivity factors.

<sup>d</sup> Bulk atomic ratio obtained from ICP analysis.

<sup>e</sup> Bulk atomic ratio obtained from EDX analysis.

WL intensities at Pt  $L_3$  and Pd K edge for all of the RGO-supported catalysts exhibit greater values than those of corresponding metal foils. Among the RGO-supported catalysts, the magnitude of the Pt WL intensity appears to increase in order of PdPt/RGO < Pd@Pt/RGO < Pt/RGO (inset of Figure 5A). This decreased WL intensities for the case of Pd-Pt bimetallic catalysts could be attributed to partial filling of the unoccupied Pt  $5d$  orbital by electron transfer from the adjacent Pd, which can also be interpreted from the electronegativity difference of Pd and Pt element with 2.20 and 2.28, respectively. Therefore, the electronic transition of  $2p \rightarrow 5d$  is suppressed. The PdPt/RGO shows the smaller Pt WL intensity than the Pd@Pt/RGO, indicating that the Pt atoms in the PdPt/RGO has a higher degree of alloying phase, which is also supported by the XPS analysis discussed above. Since the WL feature in the Pd K edge represents the transition from  $1s$  orbital to  $4d$  orbitals, the increased WL intensities observed in the bimetallic catalysts, especially in the alloyed PdPt/RGO, may suggest a less filled  $d$  band of Pd in the catalysts as shown in the inset of Figure 5B. The quantitative WL values with the edge energy analysis were summarized in Table 2.

The EXAFS spectra were collected to get the quantitative structural information on the RGO-supported catalysts. The EXAFS data in  $k$  space are displayed in Figure S8. The  $k$  space EXAFS oscillations at both Pt  $L_3$  and Pd K edge show significant amplitude reductions compared to those in Pt and Pd metal foils due to the finite size and structural disorder effects.<sup>72,73</sup> The oscillations of the Pd@Pt/RGO are slightly phase-shifted from Pt foil, which represents that there exists somewhat interaction between Pt shells and Pd atoms in the core. In contrast, the PdPt/RGO shows significant discrepancy in the phase and shapes of the  $k$  space oscillations, indicating a drastic change in the Pt local environment due to the random mixing of Pt and Pd within the nanoparticles. The Figures 6A and B represent the Fourier transformed (FT) EXAFS data and theoretical fits at the Pt  $L_3$  edge and Pd K edge, respectively. These FT-EXAFS data are characterized by the main peaks appearing between ca. 2 and 3 Å at both the Pt  $L_3$  and Pd K edge, which is likely due to the contribution from the phase-uncorrected first shells of Pt-M (M = Pt or Pd) and Pd-M interactions.<sup>74</sup> Significant differences in the FT-EXAFS spectra are clearly visible between the PdPt/RGO and Pd@Pt/RGO catalysts, showing their structures are quite different. The

**Table 2.** Electronic parameters of the catalysts measured from XANES analysis.

Catalyst	Edge	$E_0$ (eV)	WL intensity (a.u.)
Pt foil	Pt L <sub>3</sub>	11564.6	1.268
Pt/RGO		11564.9	1.367
PdPt/RGO		11564.1	1.306
Pd@Pt/RGO		11564.5	1.333
Pd foil	Pd K	24355.7	0.946
PdPt/RGO		24355.8	0.977
Pd@Pt/RGO		24355.5	0.953

structural parameters calculated from the curve-fitting analysis of EXAFS in R space are summarized in Table S1 in ESI. The Pt-Pt bond distances of PdPt/RGO and Pd@Pt/RGO are determined to be  $2.735 \pm 0.005$  Å and  $2.743 \pm 0.008$  Å, respectively. These values are smaller than that of pure Pt foil ( $2.767 \pm 0.002$  Å). The values of the Pt first shell coordination number ( $N_{\text{Pt-Pt}} + N_{\text{Pt-Pd}}$ ) for PdPt/RGO and Pd@Pt/RGO are  $9.3 \pm 0.6$  and  $7.6 \pm 0.7$ , respectively, which are significantly lower than that for bulk metal value ( $N = 12$ ), due to finite particle size of the nanoparticles with an increased fraction of surface sites. The PdPt/RGO has relatively high heterometallic coordination numbers, which are  $N_{\text{Pt-Pd}} = 3.9 \pm 0.5$  and  $N_{\text{Pd-Pt}} = 2.0 \pm 0.2$ , indicating a high degree of mixing phase of Pt and Pd at the atomic scale. The heterometallic coordination numbers in the Pd@Pt/RGO ( $N_{\text{Pt-Pd}} = 1.0 \pm 0.5$  and  $N_{\text{Pd-Pt}} = 0.5 \pm 0.3$ ) are small, indicating a limited heterometallic interactions between Pd core and Pt shell.<sup>75</sup> The XANES and EXAFS results clearly support the electronic and geometric differences between the two catalyst systems of PdPt/RGO and Pd@Pt/RGO.

The core-shell Pd@Pt/RGO catalyst was further characterized by CV, which reflects the electrochemical properties of electrocatalyst surface. The CV curves of the different catalyst samples in 0.5 M NaOH solution were collected (Figure S9). For all of the catalysts, the peaks related to hydrogen adsorption/desorption and oxide formation/reduction are clearly observed in the potential ranges of  $-0.95$  to  $-0.6$  V and  $-0.4$  to  $0.25$  V, respectively. The peak appearance at about  $-0.2$  V during the forward scan is due to the formation of the Pt hydroxide layers on the surface of the catalysts, which is a typical behavior in alkaline solutions<sup>76,77</sup>. In the voltammogram of the PdPt/RGO catalyst, a sharp cathodic peak associated with oxygen desorption at PdPt alloy nanoparticles is observed at approximately  $-0.3$  V. In addition, the CV curve of Pd@Pt/RGO is clearly similar to that of the Pt/RGO and Pt/C catalysts, which implies that the surface of the core-shell Pd@Pt particles is predominantly covered by Pt and is similar to the surface state of Pt/RGO. These CV results confirm the alloy structure of the PdPt/RGO and the core-shell structure of Pd@Pt/RGO.

The electrochemically active surface area (ECSA) of the catalysts is usually estimated using the accumulated electric charge of the hydrogen desorption region of the CV. The estimated ECSA values were found to be 40.35, 49.02, 37.55, and 29.94 m<sup>2</sup>/g for Pt/C, Pt/RGO, PdPt/RGO, and Pd@Pt/RGO, respectively.

The electrocatalytic activities of the Pt/RGO, PdPt/RGO, and Pd@Pt/RGO catalysts toward the MOR were examined by

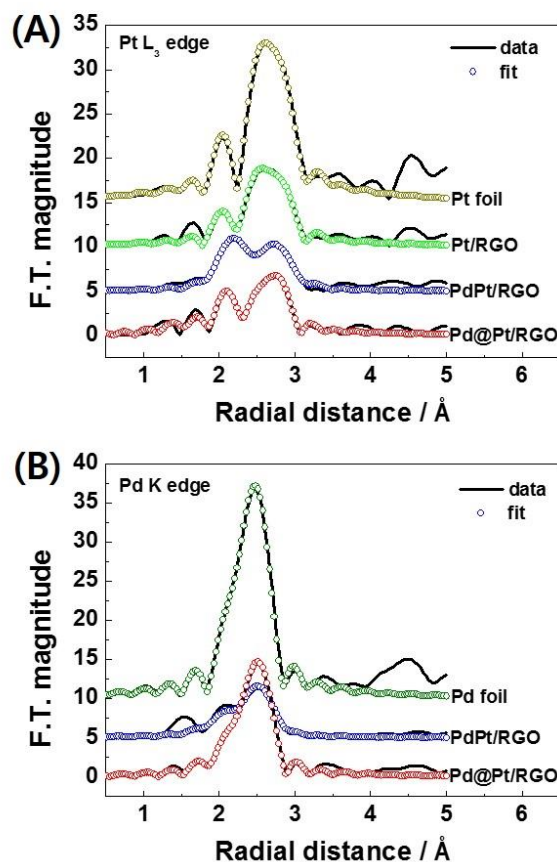


**Figure 6.** FT-EXAFS spectra of the samples (—) and fitted functions (o) at the (A) Pt L<sub>3</sub> edge and (B) Pd K edge for Pt/RGO, Pd/RGO, PdPt/RGO, and Pd@Pt/RGO with their corresponding metal foils.

CV tests in 0.5 M NaOH + 0.5 M methanol solution, as shown in Figure 7A. The current densities were normalized by the total mass of Pt and Pd. The CV curves show similar characteristic shapes with respect to the methanol oxidation peaks in the forward scan and an oxidation peak in the backward scan; the latter is attributed to the removal of the residual carbonaceous species formed during the forward scan. The Pd@Pt/RGO catalyst obviously shows the highest mass activity, with a peak current of 4972 mA mg<sup>-1</sup>, which is 3.4 times greater than that of the commercial Pt/C catalyst (1473 mA mg<sup>-1</sup>). This mass activity value is also significantly higher than those of the other RGO-supported catalysts in this work: 1.9 times greater than that of Pt/RGO (2540 mA mg<sup>-1</sup>) and 1.3 times greater than that of PdPt/RGO (3824 mA mg<sup>-1</sup>). Furthermore, the onset potential of Pd@Pt/RGO is much lower than those of the other catalysts, which also indicates substantially improved electrocatalytic activity of the Pd@Pt/RGO toward the MOR under alkaline conditions. For comparison, Pd/RGO was also prepared through the same synthetic method and examined as a catalyst for MOR (Figure S10). As a result, the Pd/RGO showed a mass activity of 1182 mA mg<sup>-1</sup>, which is the lowest value among the tested catalysts.

The CVs of MOR were also normalized by the ECSA for the comparison of different catalysts (Figure S11). The ECSA-normalized peak current density is on the order of Pd@Pt/RGO > PdPt/RGO > Pt/RGO > Pt/C, showing the similar trend to that of the mass-normalized activities.

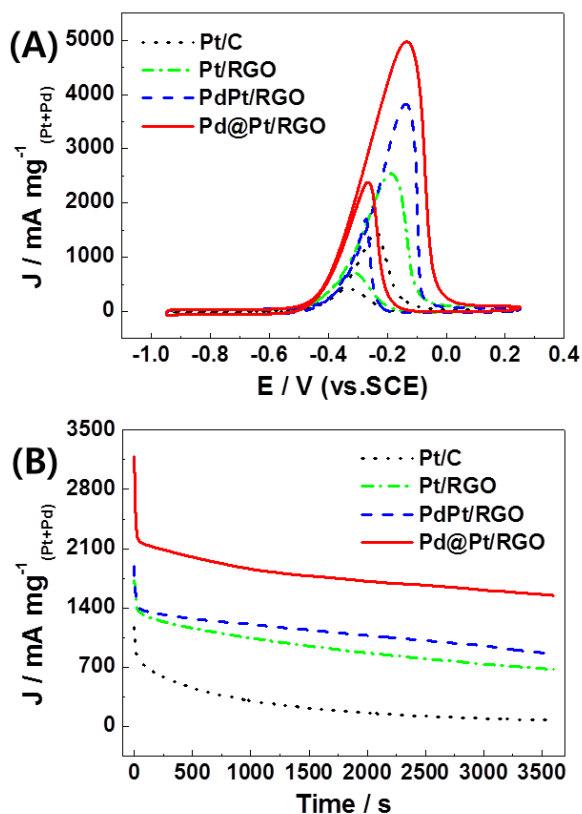


**Figure 7.** (A) CV curves of Pt/C, Pt/RGO, PdPt/RGO, and Pd@Pt/RGO in N<sub>2</sub>-saturated 0.5 M NaOH + 0.5 M methanol obtained with a scan rate of 50 mV s<sup>-1</sup>. (B) CA curves of the catalysts in 0.5 M NaOH + 0.5 M methanol at a constant voltage of -0.25 V for 3600 s.

The electrochemical activity and stability of the MOR were further evaluated by subsequent chronoamperometry (CA) tests in a solution of 0.5 M NaOH + 0.5 M methanol for 3600 s at a constant voltage of -0.25 V, as shown in Figure 7B. The Pd@Pt/RGO catalyst clearly maintains a much higher oxidation current density during the entire testing duration, which demonstrates the outstanding electrochemical performance of the Pd@Pt/RGO catalyst. The residual current densities of the Pd@Pt/RGO, PdPt/RGO, Pt/RGO, and Pt/C catalysts after 3600 s are 1549, 856, 673, and 73 mA mg<sup>-1</sup>, respectively.

The CV curves before and after the CA tests of each catalyst are shown in Figures S12A-D and the changes in peak current densities are compared in Figure 8. Remarkably, no obvious change (only ~ 1%) in MOR activity of Pd@Pt/RGO catalyst was observed after the CA test, whereas the MOR activity reductions of PdPt/RGO, Pt/RGO, and Pt/C were approximately 14%, 27%, and 35%, respectively. This result clearly indicates that the Pd@Pt/RGO catalyst is also highly stable for the MOR in alkaline media.

The enhanced stability of Pd@Pt/RGO catalyst in MOR was further confirmed by long term cyclic test (Figure S13A). The current density was normalized by the initial current to compare the decay rate. After 250 cycles, the Pd@Pt/RGO presents the normalized current of 75.4 % which is much higher than the PdPt/RGO (45.0 %), Pt/RGO (30.8 %), and Pt/C (9.6 %). Consistent with the CA results, the Pd@Pt/RGO catalyst shows the better current density than other tested catalysts. Furthermore, the morphology of Pd@Pt/RGO after

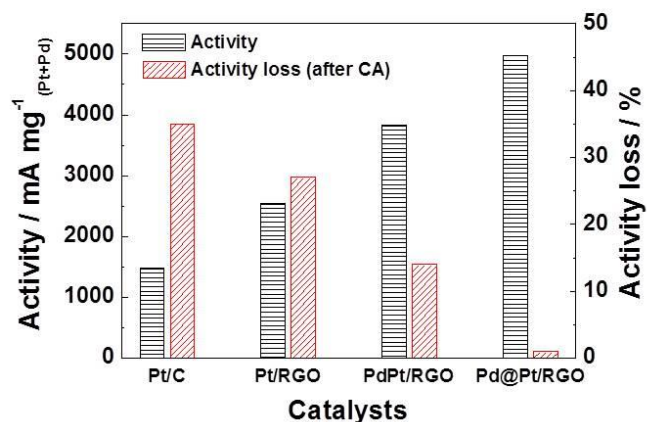


**Figure 8.** Comparison of electrocatalytic activities with different catalysts and their activity losses after CA tests.

stability test was generally retained as observed by TEM analysis (Figure S13B). From these data, we could conclude that the Pd@Pt/RGO catalyst has the superior stability.

To investigate the electron-transfer properties of the electrode systems constructed using these different catalysts, we obtained Nyquist plots at various electrode potentials using the electrochemical impedance spectroscopy (EIS) technique; the results are presented in Figures 9A-B. The smaller diameter of the arc indicates a lower charge-transfer resistance ( $R_{ct}$ ) for the MOR.<sup>78,79</sup> In comparison with the monometallic Pt/C catalyst (Figure 9A), the Pt/RGO exhibited significantly less charge transport resistance at all applied potentials. This result implies that the conductive RGO support plays a beneficial role in the charge transport compared to commonly used carbon-black supports. In the case of the RGO-supported bimetallic catalysts, the Pd@Pt/RGO catalyst showed smaller  $R_{ct}$  values than did PdPt/RGO at different electrode potentials, which indicates that the Pd@Pt/RGO has improved charge transport properties (Figure 9B). This EIS observation may provide a good rationale for the previous CV and CA results that show the enhanced electrocatalytic activity of the Pd@Pt/RGO catalyst system.

## Conclusions

In summary, bimetallic Pd@Pt core-shell or PdPt alloy particles that were supported on RGO sheets were fabricated by a simple, surfactant-free, one-pot reduction process. This process was also applied to synthesize monometallic Pt nanocrystals on the RGO support. The resulting nanocomposites were investigated using various physicochemical characterization methods, including SEM, TEM, HRTEM, EDX, XRD, Raman spectroscopy, XPS, and XAS. Among the various nanocomposites, Pd@Pt/RGO exhibited excellent electrocatalytic performance toward MOR in alkaline solution; this catalyst exhibited superior activity and enhanced electrocatalytic stability relative to those of the other catalysts tested, i.e., PdPt/RGO, Pt/RGO, and commercial Pt/C catalysts. The Pd@Pt/RGO catalyst has potential applications as a highly efficient anode catalyst for alkaline DMFCs. Moreover, we expect that this simple, inexpensive, and effective method can enable the design of various novel metal/graphene hybrid electrodes.

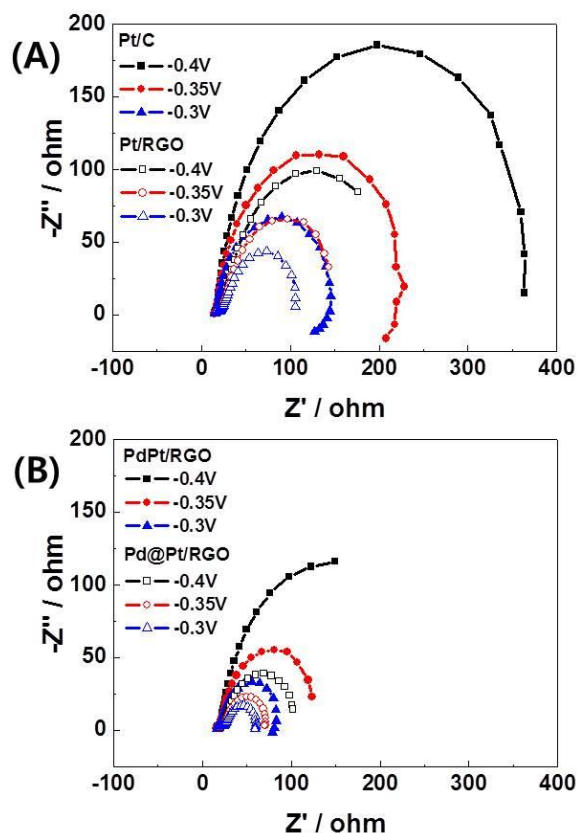


**Figure 9.** Nyquist plots of methanol oxidation on (A) monometallic Pt/C and Pt/RGO and (B) bimetallic PdPt/RGO and Pd@Pt/RGO at various electrode potentials in 0.5 M NaOH + 0.5 M methanol.

## Acknowledgements

This work was supported by the National Research Foundation (NRF) grant funded by the Korea government of the Ministry of Science, ICT & Future Planning (No. 2013029776, Mid-career Researcher Program) and the Global Frontier R&D Program on Center for Multiscale Energy System by the NRF under the MSIP (No. 0420-20130103), Korea. We also appreciate the financial supports by the Core Technology Development Program for Next-generation Solar Cells of Research Institute for Solar and Sustainable Energies (RISE), GIST.

## Notes and references

<sup>a</sup>School of Materials Science and Engineering, Gwangju Institute of Science and Technology (GIST), Gwangju, 500-712, Republic of Korea. E-mail: wbkim@gist.ac.kr; Fax: +82 62 7152304; Tel: +82 62 7152317

<sup>b</sup>Research Institute for Solar and Sustainable Energies (RISE), Gwangju Institute of Science and Technology (GIST), Gwangju, 500-712, Republic of Korea

<sup>c</sup>Department of Physics and Photon Science, Gwangju Institute of Science and Technology (GIST), Gwangju, 500-712, Republic of Korea

<sup>d</sup>Surface Technology Division, Korea Institute of Materials Science (KIMS), Changwon 641-010, Republic of Korea

†Electronic Supplementary Information (ESI) available: [Table for EXAFS fitting, SEM image, TEM images, XPS spectra, EXAFS spectra and CV data]. See DOI: 10.1039/b000000x/

- X. Zhao, M. Yin, L. Ma, L. Liang, C. Liu, J. Liao, T. Lu, and W. Xing, *Energy Environ. Sci.*, 2011, **4**, 2736.
- E. H. Yu, X. Wang, U. Krewer, L. Li, and K. Scott, *Energy Environ. Sci.*, 2012, **5**, 5668.
- V. R. Stamenkovic, B. S. Mun, M. Arenz, K. J. J. Mayrhofer, C. A. Lucas, G. Wang, P. N. Ross, and N. M. Markovic, *Nat. Mater.*, 2007, **6**, 241.
- J. H. Kim, S. M. Choi, S. H. Nam, M. H. Seo, S. H. Choi, and W. B. Kim, *Appl. Catal. B-Environ.*, 2008, **82**, 89.
- C. Hsieh and J. Lin, *J. Power Sources*, 2009, **188**, 347.
- S. Wang, N. Kristian, S. Jiang, and X. Wang, *Nanotechnology*, 2009, **20**, 025605.
- H. Wang, R. Wang, H. Li, Q. Wang, J. Kang, and Z. Lei, *Int. J. Hydrog. Energy*, 2011, **36**, 839.
- Y. Li, Z. W. Wang, C. Chiu, L. Ruan, W. Yang, Y. Yang, R. E. Palmer, and Y. Huang, *Nanoscale*, 2012, **4**, 845.
- X. Zhou and L. Fan, *Electrochim. Acta*, 2010, **55**, 8111.
- J. R. Croy, S. Mostafa, L. Hickman, H. Heinrich, and B. R. Cuenya, *Appl. Catal. A-Gen.*, 2008, **350**, 207.
- C. Bianchini and P. K. Shen, *Chem. Rev.*, 2009, **109**, 4183.
- E. J. Lim, H. J. Kim, and W. B. Kim, *Catal. Commun.*, 2012, **25**, 74.
- R. Choi, S. Choi, C. H. Choi, K. M. Nam, S. I. Woo, J. T. Park, and S. W. Han, *Chem. Eur. J.*, 2013, **19**, 8190-8198.
- H. Zhang, M. Jin, and Y. Xia, *Chem. Soc. Rev.*, 2012, **41**, 8035.
- S. M. Alia, K. O. Jensen, B. S. Pivovarov, and Y. Yan, *ACS Catal.* 2012, **2**, 858.
- K. Sasaki, H. Naohara, Y. Cai, Y. M. Choi, P. Liu, M. B. Vukmirovic, J. X. Wang, and R. R. Adzic, *Angew. Chem. Int. Ed.*, 2010, **49**, 8602.
- B. Wu and N. Zheng, *Nano Today*, 2013, **8**, 168.
- Y. Lu, Y. Jiang, H. Wu, and W. Chen, *J. Phys. Chem. C*, 2013, **117**, 2926.
- G. Chen, Y. Tan, B. Wu, G. Fu, and N. Zheng, *Chem. Commun.*, 2012, **48**, 2758.
- A. Yin, X. Min, Y. Zhang, and C. Yan, *J. Am. Chem. Soc.*, 2011, **133**, 3816.
- B. Y. Xia, H. B. Wu, X. Wang, and X. W. Lou, *J. Am. Chem. Soc.*, 2012, **134**, 13934.
- B. Y. Xia, H. B. Wu, Y. Yan, X. W. Lou, and X. Wang, *J. Am. Chem. Soc.*, 2013, **135**, 9480.
- Y. S. Kim, S. H. Nam, H. Shim, H. Ahn, M. Anand, and W. B. Kim, *Electrochem. Commun.*, 2008, **10**, 1016.
- S. Guo, S. Dong, and E. Wang, *Chem. Commun.*, 2010, **46**, 1869.
- B. Y. Xia, W. T. Ng, H. B. Wu, X. Wang, and X. W. Lou, *Angew. Chem. Int. Ed.*, 2012, **51**, 7213.
- C. Du, M. Chen, W. Wang, Q. Tan, K. Xiong, and G. Yin, *J. Power Sources*, 2013, **240**, 630.
- S. M. Alia, K. Jensen, C. Contreas, F. Garzon, B. Pivovarov, and Y. Yan, *ACS Catal.*, 2013, **3**, 358.
- Y. Kim, H. J. Kim, Y. S. Kim, S. M. Choi, M. H. Seo, and W. B. Kim, *J. Phys. Chem. C*, 2012, **116**, 18093.
- B. Y. Xia, H. B. Wu, X. Wang, and X. W. Lou, *Angew. Chem. Int. Ed.*, 2013, **52**, 12337.

- 30 S. Mourdikoudis, M. Chirea, T. Altantzis, I. Pastoriza-Santos, J. Perez-Juste, F. Silva, S. Bals, and L. M. Liz-Marzan, *Nanoscale*, 2013, **5**, 4776.
- 31 S. Patra, B. Viswanath, K. Barai, N. Ravishankar, and N. Munichandraiah, *ACS Appl. Mater. Interfaces*, 2010, **2**, 2965.
- 32 S. Guo, S. Dong, and E. Wang, *ACS Nano* 2010, **4**, 547.
- 33 C. Zhu, S. Guo, and S. Dong, *Chem. Eur. J.*, 2013, **19**, 1104.
- 34 C. Xu, Y. Liu, J. Wang, H. Geng, and H. Qiu, *ACS Appl. Mater. Interfaces*, 2011, **3**, 4626.
- 35 S. Sharma and B. G. Pollet, *J. Power Sources*, 2012, **208**, 96.
- 36 E. Yoo, T. Okata, T. Akita, M. Kohyama, J. Nakamura, and I. Honma, *Nano Lett.*, 2009, **9**, 2255.
- 37 Z. H. Sheng, H. L. Gao, W. J. Bao, F. B. Wang, and X. H. Xia, *J. Mater. Chem.*, 2012, **22**, 390.
- 38 Y. Zhang, K. Fugane, T. Mori, L. Niu, and J. Ye, *J. Mater. Chem.*, 2012, **22**, 6575.
- 39 N. Brun, S. A. Wohlgemuth, P. Osiceanu, and M. M. Titirici, *Green Chem.*, 2013, **15**, 2514.
- 40 S. Yasuda, L. Yu, J. Kim, and K. Murakoshi, *Chem. Commun.*, 2013, **49**, 9627.
- 41 S. M. Choi, M. H. Seo, H. J. Kim, and W. B. Kim, *Carbon*, 2011, **49**, 904.
- 42 S. Stankovich, D. A. Dikin, R. D. Piner, K. A. Kohlhaas, A. Kleinhammes, Y. Jia, Y. Wu, S. T. Nguyen, and R. S. Ruoff, *Carbon*, 2007, **45**, 1558.
- 43 M. J. Fernandez-Merino, L. Guardia, J. I. Paredes, S. Villar-Rodil, P. Solis-Fernandez, A. Martinez-Alonso, and J. M. D. Tascon, *J. Phys. Chem. C*, 2010, **114**, 6426.
- 44 S. Kim, G. H. Jeong, D. Choi, S. Yoon, H. B. Jeon, S. Lee, and S. Kim, *J. Colloid Interface Sci.*, 2013, **389**, 85.
- 45 S. M. Choi, M. H. Seo, H. J. Kim, and W. B. Kim, *Synth. Met.*, 2011, **161**, 2405.
- 46 M. S. Nashner, A. I. Frenkel, D. Somerville, C. W. Hills, J. R. Shapley, and R. G. Nuzzo, *J. Am. Chem. Soc.*, 1998, **120**, 8093.
- 47 B. Ravel and M. Newville, *J. Synchrotron Radiat.*, 2005, **12**, 537.
- 48 X. Chen, Z. Cai, X. Chen, and M. Oyama, *J. Mater. Chem. A*, 2014, **2**, 315.
- 49 S. C. Sahu, A. K. Samantara, A. Dash, R. R. Juluri, R. K. Sahu, B. K. Mishra, and B. K. Jena, *Nano Res.*, 2013, **6**, 635.
- 50 C. H. Kuo, and M. H. Huang, *Langmuir*, 2005, **21**, 2012.
- 51 H. Lee, S. E. Habas, S. Kweskin, D. Butcher, G. A. Somorjai, and P. Yang, *Angew. Chem. Int. Ed.*, 2006, **45**, 7824.
- 52 L. Shi, A. Wang, T. Zhang, B. Zhang, D. Su, H. Li, and Y. Song, *J. Phys. Chem. C*, 2013, **117**, 12526.
- 53 M. Jiang, B. Kim, J. Tao, P. H. C. Camargo, C. Ma, Y. Zhu, and Y. Xia, *Nanoscale*, 2010, **2**, 2406.
- 54 L. Wang, and Y. Yamauchi, *Chem. Asian J.*, 2010, **5**, 2493.
- 55 H. Feng, B. Wang, L. Tan, N. Chen, N. Wang, and B. Chen, *J. Power Sources*, 2014, **246**, 621.
- 56 M. Seredych, C. Petit, A. V. Tamashauskyy, T. J. Bandosz, *Carbon*, 2009, **47**, 445.
- 57 Z. Huang, H. Zhou, C. Li, F. Zeng, C. Fu, and Y. Kuang, *J. Mater. Chem.*, 2012, **22**, 1781.
- 58 G. Zhang, Z. Shao, W. Lu, F. Xie, X. Qin, and B. Yi, *Electrochim. Acta*, 2013, **103**, 66.
- 59 X. Li, S. Park, and B. N. Popov, *J. Power Sources*, 2010, **195**, 445.
- 60 V. Radmilovic, H. A. Gasteiger, and P. N. Ross, *J. Catal.*, 1995, **154**, 98.
- 61 D. R. Dreyer, S. Park, C. W. Bielawski, and R. S. Ruoff, *Chem. Soc. Rev.*, 2010, **39**, 228.
- 62 G. K. Ramesha and S. Sampath, *J. Phys. Chem. C*, 2009, **113**, 7985.
- 63 J. Shen, B. Yan, M. Shi, H. Ma, N. Li, and M. Ye, *J. Mater. Chem.*, 2011, **21**, 3415.
- 64 J. Zhang, H. Yang, G. Shen, P. Cheng, J. Zhang, S. Guo, *Chem. Commun.*, 2010, **46**, 1112.
- 65 N. A. Jumar, S. Gambarelli, F. Duclairoir, G. Bidan, and L. Dubois, *J. Mater. Chem. A*, 2013, **1**, 2789.
- 66 K. H. Lee, B. Lee, S. Hwang, J. Lee, H. Cheong, O. Kwon, K. Shin, and N. H. Hur, *Carbon*, 2014, **69**, 327.
- 67 B. Wang, X. Wang, W. Lou, and J. Hao, *New J. Chem.*, 2012, **36**, 1684.
- 68 Z. Wang, P. Li, Y. Chen, J. He, B. Zheng, J. Liu, and F. Qi, *Mater. Lett.*, 2014, **116**, 416.
- 69 H. Shin, K. K. Kim, A. Benayad, S. Yoon, H. K. Park, I. Jung, M. H. Jin, H. Jeong, J. M. Kim, J. Choi, and Y. H. Lee, *Adv. Funct. Mater.*, 2009, **19**, 1987.
- 70 T. K. Sham, *Phys. Rev. B*, 1985, **31**, 1888.
- 71 H. J. Kim, S. M. Choi, S. H. Nam, M. H. Seo, and W. B. Kim, *Appl. Catal. A-Gen.*, 2009, **352**, 145.
- 72 M. S. Nashner, A. I. Frenkel, D. L. Adler, J. R. Shapley, and R. G. Nuzzo, *J. Am. Chem. Soc.*, 1997, **119**, 7760.
- 73 A. I. Frenkel, C. W. Hills, and R. G. Nuzzo, *J. Phys. Chem. B*, 2001, **105**, 12689.
- 74 S. Mukerjee, S. Srinivasan, and M. P. Soriaga, *J. Phys. Chem.*, 1995, **99**, 4577.
- 75 B. Hwang, L. S. Sarma, J. Chen, C. Chen, S. Shih, G. Wang, D. Liu, J. Lee, and M. Tang, *J. Am. Chem. Soc.*, 2005, **127**, 11140.
- 76 W. Vielstich, A. Lamm, and H. A. Gasteiger, *Handbook of Fuel Cells*, John Wiley & Sons, England, 2003, **vol. 2**, ch. 14, p. 155.
- 77 A. C. Garcia, and E. A. Ticianelli, *Electrochim. Acta*, 2013, **106**, 453.
- 78 Y. S. Kim, H. S. Jang, and W. B. Kim, *J. Mater. Chem.*, 2010, **20**, 7859.
- 79 Z. Wang, G. Yin, Y. Shao, B. Yang, P. Shi, and P. Feng, *J. Power sources*. 2007, **165**, 9.